UNIVERSITY OF SZEGED

SUMMARY OF THE PH.D. THESIS

# Image Quality Improvement in Computed and Binary Tomography

*Author:*
**Gábor LÉKÓ**

*Supervisor:*
**Péter BALÁZS, Ph.D.**
*associate professor*

Doctoral School of Computer Science
Department of Image Processing and Computer Graphics
Faculty of Science and Informatics
University of Szeged, Hungary


Szeged, 2020

# 1 Introduction

The goal of tomographic reconstruction is to discover the inner structure of objects using their projections in a slice-by-slice manner. Most often, the projections are produced by X-rays. Measuring the attenuation of the beams passing through the object can provide information on the density of the materials along the paths of the beams (see Fig. 1a for illustration). Collecting such projection data from many angles, one can produce an image showing the inner structure of the object [4, 7]. Computed Tomography (CT) is a widely used tool in different fields, such as medical imaging, non-destructive testing (NDT), material characterization, crystallography, etc. to analyze the interior of the subject of investigation.

Discrete Tomography (DT) [5, 6] uses the prior information that the cross-section image to be reconstructed contains only a few different intensities which are known in advance. Exploiting this prior knowledge, a smaller set of projections is sufficient for a reconstruction with an acceptable quality.

Binary Tomography (BT) is a more restricted variant of DT. In this case, every single pixel of the image to be reconstructed can take only two different intensities. In practice, objects corresponding to these images must be made of a homogeneous material.

The dissertation addresses the Author's research in the field of CT and BT. Our main aim was to improve reconstruction quality by developing novel algorithms and improving previous approaches in the research fields of selecting the most informative projection angles, automatic selection of the tube voltage of a CT scanner, and binarizing already reconstructed CT slices using Convolutional Neural Networks.

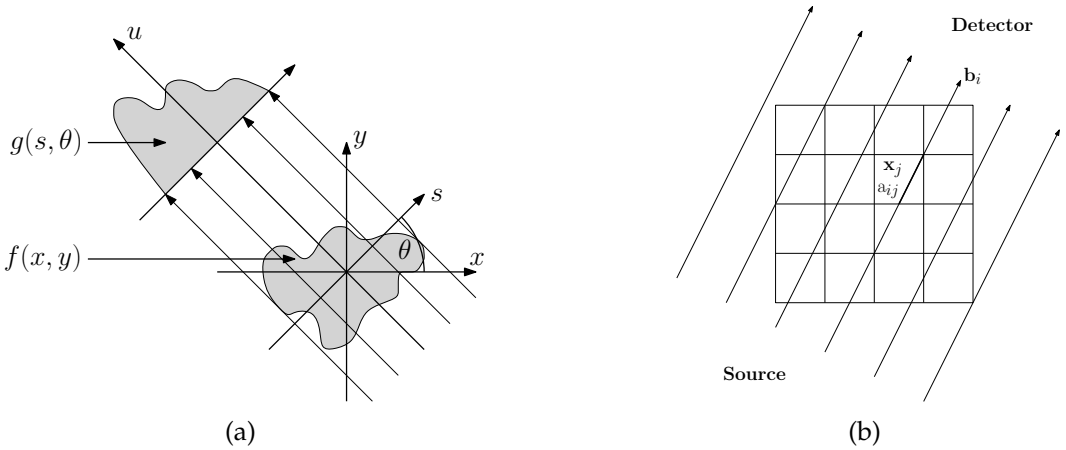


(a) (b)

Figure 1: (a) Acquisition of a projection. (b) Equation system-based representation of the parallel-beam projection geometry.

# 2 Formulation of the reconstruction problem

Due to the small number of projections, typically available in DT, the reconstruction is mainly solved by one of the algebraic approaches. The idea is to describe the connections between projections and pixels using equations. Assuming that the size of the image to be reconstructed is $n \times n$ ($N = n^2$), the reconstruction problem can be described as a system of linear equations (see Fig. 1b for illustration):

$$\mathbf{A}\mathbf{x} = \mathbf{b}, \quad \mathbf{A} \in \mathbb{R}^{m \times N}, \quad \mathbf{x} \in \mathbb{R}^{N}, \quad \mathbf{b} \in \mathbb{R}^{m}, \tag{1}$$

where $\mathbf{x}$ is the vector of all $N$ unknown image pixels, $\mathbf{b}$ is the vector of all $m$ measured projection values ($m$ is the total number of projection lines used), and $\mathbf{A}$ describes the projection geometry with all $a_{i,j}$ elements giving the length of the line segment of the $i$th projection line through the

$j$th pixel. If we want to further limit this formulation into the binary reconstruction problem, we have to add a new restriction to $\mathbf{x}$, which is $\mathbf{x} \in \{0,1\}^N$. This way $\mathbf{x}$ is forced to contain only $\{0,1\}$ values.

# 3 Offline Projection Selection Algorithms and their Scale Invariance

In BT, we use the prior information that the object consists of a single material, and the gaps are filled with air. In some cases, this constraint can lead to accurate results, even from just 4–8 projections. In their paper [16], Nagy et al. noted that when using a low number of projections, the accuracy of a binary reconstruction can depend on the projection angles. Further investigated in [24], this phenomenon was found to depend on the structure of the object of study. Thus, further attention was paid on how the "most informative" projections can be found. Projection selection methods can be classified as online and offline ones. In this thesis point, we are going to focus on the latter.

In the offline case, a blueprint image of the object to be reconstructed is given (which is rather typical, e.g., in industrial NDT), on which the whole projection data can be simulated, and the proper projection set can be identified. In this context, the projections are not always gathered by real physical measurements. They can be simulated using a golden standard (ground-truth or blueprint) that is often available in industrial quality testing, e.g., as a CAD model. In [25], several approaches have been published aiming to find good projection angles for BT, all of them reducing the search space of projection sets in various ways.

In this thesis point, we suggest sequential search methods [20] to find projection angles with high information content and analyze the behavior of these methods under serious resolution down-scaling.

## 3.1 Projection selection algorithms

We first recall three projection selection strategies from [25] that serve as references for comparison with our suggested methods. The approaches given in [25] are the best performing state-of-the-art methods in this field.

One of the simplest methods is when the projection angles are distributed proportionally, with equiangular spacing. One can distinguish two variants. In the first case, the starting angle is positioned to $0^\circ$. As an improved version, in the second case, all the integer starting angles are analyzed between $0^\circ$ and $\left[\frac{180}{p}\right]^\circ$, where $p$ is the number of projections. In the end, the angle set ensuring the best quality (with the smallest Relative Mean Error (RME) value) is kept. The authors of [25] referred to these methods as *Naive* and *EquiAng* angle selections, respectively, and so do we.

To handle the issue of selecting arbitrary angles, in [25], the authors presented the problem as an energy minimization task. An optimal set of angles must satisfy

$$RME(\mathbf{x}^*, \mathbf{x}^{S^*}) = \min_S RME(\mathbf{x}^*, \mathbf{x}^S)\,, \tag{2}$$

where $S$ is an arbitrary set of angles, $S^*$ is the optimal set of angles, $\mathbf{x}^S$ and $\mathbf{x}^{S^*}$ are the reconstructions from the projections with $S$ and $S^*$ angle sets, respectively. Simulated annealing [14] was proposed for the minimization. We refer to this method as *SA*.

## 3.2 Proposed sequential search methods

By the observation that projections can serve as features of the image to reconstruct, we examined numerous types of feature selection algorithms, following the summary of [15]. According to this examination, the floating search methods [20] seemed to be the best options in this area.

Other algorithms contain too much randomization, use exhaustive search, or tree structure which makes them hardly applicable for this task.

First, we investigated and modified the forward and backward sequential selection methods (*SFS* and *SBS*) to serve as projection selection methods. In the case of *SFS*, the process starts with the initialization of a feature subset. Then it iteratively adds features to the initial subset. In the case of *SBS*, the initial feature set contains all the features. Then, iteratively, one feature will be removed from the set, namely whose deletion causes the least loss in the evaluation measure. Both processes stop when no improvement happens in the evaluation measure in the last $t$ steps (where $t$ is a predefined threshold variable) or all the necessary number of features has been added to the set or deleted from the set, respectively.

Both *SFS* and *SBS* suffer from a so-called "nesting effect". It means that in *SFS*, the features once selected cannot be later discarded, while in *SBS*, the discarded features cannot be reselected. The result is that the methods are only suboptimal. With a further investigation, we combined the *SFFS* and *SBFS* (Sequential Floating Forward/Backward Search) methods together and created our *Refinement* algorithm. In our interpretation, the algorithm starts with an initial angle set, which can be the output of any type of projection selection algorithm, and then we apply the *Refinement*. Depending on which algorithm is used as the first step, we refer to these algorithms as *NaiveR*, *EquiAngR*, *SAR*, *SFSR*, and *SBSR*, i.e., the original name is extended with the letter *R* (*R* is for *Refinement*). The *Refinement* algorithm can be seen in Alg. 1, which is capable of refining the result of the output of any other algorithm.

**Algorithm 1:** Angle selection with *Refinement*

let $S$ be the set of the actual angles - output of an angle selection algorithm
fix$\Theta \leftarrow$ the last element inserted into $S$
**repeat**
  **for all** angle $\theta \in S \setminus \{\text{fix}\Theta\}$ **do**
    calculate $RME(\mathbf{x}^*, \mathbf{x}^{S\setminus\{\theta\}})$
    $\theta_{min} \leftarrow$ angle corresponding to the smallest $RME$ value
  **end for**
  $S \leftarrow S \setminus \{\theta_{min}\}$
  **for** $\theta \leftarrow 0$ to 179 **do**
    calculate $RME(\mathbf{x}^*, \mathbf{x}^{S\cup\{\theta\}})$
    $\theta_{min} \leftarrow$ angle corresponding to the smallest $RME$ value
  **end for**
  $S \leftarrow S \cup \{\theta_{min}\}$
  fix$\Theta \leftarrow \theta_{min}$
**until** the $RME$ cannot be decreased any more.

### 3.3 Scale Invariance in Projection Selection

#### 3.3.1 Technique (*T1*): Resizing the image

In industrial NDT, often hundreds or thousands of projections of the examined object are acquired, and the number of detector pixels can also be of the same magnitude. This allows us to reconstruct a high-quality image from its projections. However, if we want to apply a projection selection method on the reconstructed image, it could take an unacceptably long time due to the high resolution. To speed up this process, one can downscale the reconstructed image and then apply the projection selection algorithm just after this step.

By reducing the resolution, one may lose information, and the object in the image may deform due to structural and topological changes. For projection selection, however, we do not

need that much and detailed projection information. If the image preserves the most specific structural information about its content, it is completely enough to find the most informative angles. For downscaling, we used the Gaussian pyramid.

#### 3.3.2 Technique (*T2*): Summing the projection values

Another possible technique preserves the original size of the blueprint image and takes the normalized sum of every $d$ neighboring projection value, where $d$ will specify the magnitude of reduction:

$$D_l(i) = \frac{\sum_{j=d\cdot i+1}^{j<d\cdot i+d} D_{l-1}(j)}{d^2}, \quad i = 0, \ldots, m_l - 1\,. \tag{3}$$

Here $D_l$ represents the new projection vector and $m_l$ is the number of the detectors on the $l$th level. For example, if we sum every $2nd$ neighboring projection value, we halve the size of the projection vector and thus also the size of the sinogram.

#### 3.3.3 Perimetric complexity

Finding the connection between the characteristics of objects and how similar they are in the sense of direction dependency is an actively studied area of research. For that, a formula is needed that tells us whether two objects share the same set of most informative angles. In our case, this is also an important question since we want to predict how much we can rescale an image still preserving the main characteristics of its direction dependency. In [29], the author proposed a measure named perimetric complexity to describe the complexity of a binary digital image. Using this measure, we can determine which is the lowest "safe" resolution where we have to stop the downscaling. Perimetric complexity is also useful to predict how many projections one will need for a reconstruction to keep the RME value below a specified threshold.

### 3.4 Experimental studies and results

We conducted several experiments on binary software phantom images. We chose to use the thresholded version of the Simultaneous Iterative Reconstruction Technique (TSIRT). Our dataset consisted of 22 structurally and topologically different phantoms. For the comparison of the different projection selection algorithms, we used the software phantoms with a size of $256 \times 256$ pixels. For the scale invariance case, we generated the same phantoms with the side length of 16, 32, 64, 128, 256, 512, 1024, and 2048 pixels.

From all the different projection selection algorithms, *SFSR* had the ultimate smallest average in RME. However, all the other algorithms extended with *Refinement* were really close to that result, and all the *Refinement*-extended algorithms provided better results than their original (non-extended) versions.

We noticed that the original (previously published) equiangular methods (*Naive* and *EquiAng*) were fast but provided really weak quality reconstructions. However, even these algorithms could provide angle sets with acceptable quality when they were extended with our *Refinement* method, and still in a very short time. Furthermore, these algorithms are completely deterministic, while the results of *SA*, *SAR*, *SFS* and *SFSR* really depend on the random initialization. One can draw the conclusion that applying the *Refinement* step, *NaiveR* and *EquiAngR* become very competitive against the other algorithms, considering their good quality and fast execution time.

In the case of analyzing scale invariance, first, we tested the *T1* approach (resizing the image). Investigating the equiangular approaches, it was discernible that the RME values of the highest resolution images were the smallest, and these values increased (non-decreased) as the size of the image decreased in almost every case. The RME values, however, were really close

to each other. We noticed a significant difference only in the case of size $16 \times 16$. In the non-equiangular case, the RME values were not that close to each other as they had been in the equiangular case since the algorithm has more freedom during the selection. We observed that it is safer to stop downscaling when the size of $64 \times 64$ is reached. We showed that we could reduce the phantoms radically and still achieve projection sets to reconstruct the images with almost the same quality as in the original case.

Furthermore, we also tested theory *T2* in similar experiments as it was detailed above for *T1* and deduced very similar (almost same) properties. Thus, we determine that summing the projection values - i.e., reducing the number of detectors - can be applied as successfully as resizing the blueprint image.

The findings of this thesis point have been published in a conference proceedings [10] and in a journal paper [9].

# 4 Reconstruction Uncertainty in BT and CT

Adaptive (online) approaches determine the successive angles during the acquisition, based on the already available projection information. These types of projection selection algorithms allow dense sampling in the information-rich areas and sparse sampling in the information-poor areas. Even with the properly selected acquisition angles, the low number of projections turns the reconstruction task into an ill-posed problem, having various possible solutions. This lack of information produces errors in the reconstructions because we cannot determine the exact pixel values. Two research groups simultaneously investigated the theory of pixel uncertainty in discrete reconstructed images. They introduced two different approaches for measuring the variability of reconstructions.

In the first part of this thesis point, based on previous studies, we provide two projection selection methods for binary reconstruction that use the reconstruction uncertainty [28] of the available projections to choose the next angle. The first one is an offline method, which modifies the *SFSR* algorithm presented in *Section 3.2*, and the second one is an adaptive method based on [3]. In the second part of this thesis point, further examining the presence of uncertainty using the experience gained studying [28], we define a grayscale uncertainty measure and examine its behavior with different projection sets.

## 4.1 Binary uncertainty in projection selection

We can determine the uncertainty of the reconstruction using the results of [28] that we shortly recall here. Due to the incomplete information in the projection data, there can be several solutions of Eq. (1) in which the pixel values may vary. Knowing all the reconstructions we could calculate the probability of $x_j$ $(j = 1, \ldots, N)$ taking the value $x_j = 1$, by

$$p_j = \frac{\mathcal{N}_{\mathbf{b}}^{\mathbf{A}}(x_j = 1)}{\mathcal{N}_{\mathbf{b}}^{\mathbf{A}}} , \tag{4}$$

where $\mathcal{N}_{\mathbf{b}}^{\mathbf{A}}$ denotes the number of solutions of Eq. (1) and $\mathcal{N}_{\mathbf{b}}^{\mathbf{A}}(x_j = 1)$ stands for the number of binary solutions with $x_j = 1$. Given the probabilities, we can determine the uncertainty of pixel $x_j$ as

$$\mathcal{H}(x_j) = -(p_j \log_2(p_j) + (\bar{p}_j) \log_2(\bar{p}_j)) , \tag{5}$$

where $\bar{p}_j = 1 - p_j$. Taking an image and indicating all the pixels with their uncertainty values, we get the entropy map of the reconstruction. Furthermore, we can also calculate the global uncertainty of the whole reconstruction by summing the pixel uncertainties as

$$\mathcal{U}(\mathbf{x}) = \frac{\sum_{i=j}^{N} \mathcal{H}(x_j)}{\frac{1}{r} \sum_{i=1}^{m} b_i} , \tag{6}$$

where $r$ is the number of projections. Calculating Eq. (6) needs an unreasonable amount of processing time in practice since all the reconstructions satisfying the projection set have to be generated. To produce the entropy map of the solution, we substitute the probability variables in Eq. (5) with the pixel values of the reconstructed image, provided by the SIRT algorithm.

#### 4.1.1 Proposed offline method

In *Section 3.2*, we proposed the *SFSR* algorithm for projection selection. The method being proposed here uses the same methodology. The only difference is that all of the RME calculations were replaced with global uncertainty (Eq. 6) calculations and uncertainty was used for the optimization, i.e., no blueprint data was used for selecting the most informative angles, only the uncertainty of the reconstructed image itself. We refer to the modified global uncertainty based *SFSR* method as *SFSR-UNC*.

#### 4.1.2 Proposed online method

In [3], the authors proposed two adaptive angle selection algorithms. These are a spectral richness based method, which selects the projections based on the spatial spectral richness of the image function (*Alg1*), and a reconstruction error based selection (*Alg2*). We modified *Alg2* by replacing the error function with

$$E_k = \log_{10}(\sum_{j=1}^{N} |\mathcal{H}(x_j^{(k)}) - \mathcal{H}(x_j^{(k-1)})|^2) \ , \tag{7}$$

and modified steps 1 and 5 of the original *Alg2* accordingly, to use this measure when evaluating the projection angle candidates. Then, in each iteration, the candidate ensuring the biggest decrease in reconstruction uncertainty is selected. We will refer to this algorithm as *Alg2-UNC*.

#### 4.1.3 Experimental results

To test the projection selection algorithms, we used the same phantoms and settings that were used in the previous thesis point. First, *SFSR-UNC* was compared to the original *SFSR*, then, *Alg2-UNC* to the already published methods (*Alg1*, *Alg2*, *Naive*) using experimental tests on the software phantom images. We found that our former method was able to provide approximately as accurate reconstruction results as the method that used blueprint images to find the optimal set of projections. In the latter case, we found that *Alg2-UNC* could outperform the state-of-the-art algorithms and provided good alternative solutions for selecting projection angles.

### 4.2 Grayscale uncertainty

Here, we provide a measurement of the uncertainty of continuous reconstructions. For that, we introduce some notation and definitions.

#### 4.2.1 Definition of the uncertainty

Let $\mathcal{N} = \{1, 2, \ldots, N\}$ and $\mathcal{M} = \{1, 2, \ldots, m\}$. Moreover, let $\mathbf{0}_N$ denote the column vector with

$$(\mathbf{0}_N)_k = 0 \ , \ \forall k \in \mathcal{N} \ . \tag{8}$$

Furthermore let $\mathbf{e}_{N,i}$ denote the column vector such that

$$(\mathbf{e}_{N,i})_k = \begin{cases} 1, & \text{if } k = i \ , \\ 0, & \text{if } k \neq i \end{cases} \qquad \forall k \in \mathcal{N} \ . \tag{9}$$

Now we can define the core concept of the uncertainty measure.

**Definition 1.** *For any* $\mathbf{A}$ *projection matrix let the i-th perturbed reconstruction of* $\mathbf{A}$ *be*

$$\mathcal{P}_{\mathbf{A}}(i) = \arg\min_{\mathbf{x}} \{ \|\mathbf{x} - \mathbf{e}_{N,i}\| \;\mid\; \mathbf{A}\mathbf{x} = \mathbf{0}_m,\ \mathbf{x} \in \mathbb{R}^N \} \,. \tag{10}$$

**Definition 2.** *Given a projection matrix* $\mathbf{A}$*, let the uncertainty of the* $x_i$ *pixel be*

$$\mathcal{U}_{\mathbf{A}}(i) = \frac{\|\mathcal{P}_{\mathbf{A}}(i)\|_2}{\|\mathbf{e}_{N,i} - \mathcal{P}_{\mathbf{A}}(i)\|_2} \,. \tag{11}$$

### 4.3 Bounds of pixel values

Using the bound on the slopes of the hyperplane of solutions, we can give bounds on the pixel values in the reconstructions. Here, we provide two possible bounds.

**Lemma 1.** *For any* $x_k$

$$x_i \leq \min_{j \in \mathcal{M}} \frac{b_j}{a_{j,i}} \,. \tag{12}$$

**Theorem 1.** *Let* $\hat{\mathbf{x}} \in \mathbb{R}^N_{\geq 0}$ *be a solution of* $\mathbf{A}\mathbf{x} = \mathbf{b}$*, and define*

$$\mathcal{L}_{\mathbf{A}}(i) = \min_{j \in \mathcal{M}} \frac{b_j}{a_{j,i}} \tag{13}$$

*and*

$$\mathcal{D}_{\mathbf{A}}(i) = \sqrt{\sum_{k \in \mathcal{N} \setminus \{i\}} (\mathcal{L}_{\mathbf{A}}(k))^2} \,. \tag{14}$$

*Then, for any* $\mathbf{y} \in \mathbb{R}^n_{\geq 0}$ *reconstruction and any* $i \in \mathcal{N}$ *index*

$$\hat{x}_i - \mathcal{U}_{\mathbf{A}}(i) \cdot \mathcal{D}_{\mathbf{A}}(i) \;\leq\; y_i \;\leq\; \hat{x}_i + \mathcal{U}_{\mathbf{A}}(i) \cdot \mathcal{D}_{\mathbf{A}}(i) \,. \tag{15}$$

#### 4.3.1 Connection of reconstruction error and perturbed reconstructions

Assume that we have $\mathbf{x}^0$, $\hat{\mathbf{x}}$, and $\mathbf{x}^*$ as follows.

- $\mathbf{x}^0 \in \mathbb{R}^N$: is a starting point for seeking a solution.
- $\hat{\mathbf{x}}$: is a reconstruction closest to the $\mathbf{x}^0$ starting position in a euclidean manner, i.e.,

$$\hat{\mathbf{x}} = \arg\min_{\mathbf{x}} \left( \|\mathbf{x} - \mathbf{x}^0\| \;\mid\; \mathbf{A}\mathbf{x} = \mathbf{b},\ \mathbf{x} \in \mathbb{R}^N \right) \,. \tag{16}$$

- $\mathbf{x}^*$: is the expected image, i.e., the image of the original object of study.

From the definitions of $\mathbf{x}^0$, $\hat{\mathbf{x}}$, and $\mathbf{x}^*$, we define two new values. Let $\mathcal{E}_1$ be the error of the above reconstruction calculated by

$$\mathcal{E}_1 = \hat{\mathbf{x}} - \mathbf{x}^* \,. \tag{17}$$

Furthermore, we define the $\mathcal{E}_2$ weighted sum based on the perturbed reconstructions and the $\mathbf{x}^0$ base point as

$$\mathcal{E}_2 = \sum_{i=1}^{N} \left( \mathcal{P}_{\mathbf{A}}(i)(\mathbf{x}^0_i - \mathbf{x}^*_i) \right) \,. \tag{18}$$

Both $\mathcal{E}_1$ and $\mathcal{E}_2$ are vectors and by definition

$$\mathbf{A}\mathcal{E}_1 = \mathbf{A}\mathcal{E}_2 = \mathbf{0}_m \,. \tag{19}$$

We state that the error of the above-defined $\hat{\mathbf{x}}$ reconstruction can directly be determined if we know the $\mathbf{x}^*$ ideal reconstruction and the $\mathbf{x}^0$ base point.

**Theorem 2.** *Given an equation system of the form* (1) *and* $\mathbf{x}^*$, $\mathbf{x}^0$, $\hat{\mathbf{x}}$ *points and* $\mathcal{E}_1$, $\mathcal{E}_2$ *vectors defined above, then*

$$\mathcal{E}_1 = \mathcal{E}_2 \,. \tag{20}$$

#### 4.3.2 Experimental validation

To investigate the uncertainty, the bounds, and the errors from a practical point of view, we conducted experiments on different images. Our database consisted of 7 phantoms with different structural complexity, each with a size of $64 \times 64$ pixels and an intensity range of [0,1].

To show that the defined uncertainty formula can provide information about the variability of the reconstructed pixel values, we performed hundreds of Conjugate Gradient Least Squares (CGLS) reconstructions with randomly initialized starting images. These reconstructed images were used to calculate the standard deviation on a bigger image set.

For a certain phantom, we concatenated the standard deviation maps into one matrix for all the predefined projection numbers and did the same with the uncertainty maps. Then, we calculated the correlation between these "montage" images. This way, 7 comparisons were made (based on the 7 test images). The correlation values were around 0.8, which indicated a reliable correspondence between the uncertainty measure and the deviation of pixel values in reconstructions. We argue that the correlation was not higher only because the pixel values in our random reconstructions were not from uniform distribution.

Using one random reconstruction from all the phantoms with a different number of projections (created with bounded SIRT), we also analyzed the range of the bounds given in Lemma 1 and Theorem 1. In the case of Lemma 1, we observed that as the projection number increased, the bounds were getting closer and closer to the x-axis. In the case of a low number of projections, the bounds of Theorem 1 were far from each other, and as the projection number increased, the bounds were approximating each other. We performed some tests to evaluate our upper and lower bounds (based on Theorem 1) in practical reconstruction scenarios. Our experiments proved that the theoretical upper and lower bounds can sufficiently limit the pixel intensities for all the phantoms with different numbers of projections.

In a further investigation, we compared $\mathcal{E}_1$ (Eq. 17) and $\mathcal{E}_2$ (Eq. 18) for all the phantoms with all the different predefined number of projections to prove their similarity. Calculating $|\mathbf{E}_1 - \mathbf{E}_2|$, all the values were close to zero ($10^{-4} - 10^{-6}$). We remark that these extremely small values represent zeros. According to our findings, these non-zero values are present due to rounding errors in the reconstruction algorithms and the fact that the reconstructions are only approximate solutions with some tolerance.

The findings of this thesis point have been published in three conference proceedings [12, 13, 27] and are submitted as a journal paper [26].

## 5 Adaptive Automatic Tube Voltage Selection for CT

CT is one of the most frequently used modalities in radiodiagnostics and NDT. However, undergoing multiple high radiation dose examinations may cause adverse health effects, even lethal diseases in the human body. Besides, high radiation consumes a lot of energy. When using a constant energy spectrum, the investigation of elongated objects may be problematic. Using too low energy, the photons cannot penetrate the object in the direction of elongation. On the other hand, too high energy can cause the photons to traverse the object without significant attenuation, in the direction perpendicular to the elongation of the object. A solution could be to use different energy levels when producing projections from different directions.

In this thesis point, our aim is to provide an adaptive tube voltage selection method. In this context, "adaptive" means that the tube voltage will be re-selected during the acquisition, projection-by-projection. To the best of our knowledge, this is the first approach that attempts

to select tube voltage on-the-fly based only on projection (sinogram) information. This approach could be effectively applied, especially in the case of elongated objects.

### 5.1 Proposed methods

First, we need a figure of merit to quantitatively evaluate the radiation used, more precisely, the projection images produced. After experimenting with different quality measures, we narrowed down the list of possible options and chose *transmission*, which describes the ratio between the minimal and the maximal X-ray intensity at the detector. In our experiments, 20% proved to be a good choice.

Our proposed voltage selection method is described in Alg. 2. As a first part (Lines 2-7 of Alg. 2), we acquire the first projection on all the different predefined energy levels. Then the energy level with the closest transmission value to the optimum will be chosen for further acquisitions. In the second part (Lines 9-19 of Alg. 2), we acquire a projection on the previously chosen energy level. If its transmission value is in a tolerance distance to the optimum, then we stay on the current energy level. Otherwise, if it is out of the acceptable range, then we step to a higher/lower energy level for the next projection. This second part is repeated until the predefined number of projections is reached. This way, based on the shape of the object, the resulting sinogram may contain projections from different energy levels. Thus, one can collect the most informative projections (energy levels) belonging to the given angles. We will refer to the sinogram obtained this way as the *adaptive sinogram*.

**Algorithm 2:** Voltage selection

**Require:** $\mathbf{tr_{opt}}$ - optimal transmission; $\mathbf{tr_{tol}}$ - tolerance for the transmission level; **TVL** - set of predefined tube voltage levels; **S** - set of predefined angles

1: $\mathbf{tr_{opt}} \leftarrow 0.2$, $\mathbf{tr_{tol}} \leftarrow 0.25$
2: **for all** $lvl \in$ **TVL do**
3: acquire projection from starting angle on $lvl$
4: $closest_{lvl} \leftarrow lvl$ with the closest transmission value to $\mathbf{tr_{opt}}$
5: $closest_{pr} \leftarrow$ projection acquired on $closest_{lvl}$
6: $closest_{tr} \leftarrow$ transmission value of $closest_{pr}$
7: **end for**
8: $sinogram_{opt} \leftarrow sinogram_{opt} \cup closest_{pr}$
9: **for all** angle $\theta \in$ **S do**
10: $actual_{pr} \leftarrow$ acquire projection from angle $\theta$ on $closest_{lvl}$
11: $sinogram_{opt} \leftarrow sinogram_{opt} \cup actual_{pr}$
12: **if** $|\mathbf{tr_{opt}} - closest_{tr}| \geq \mathbf{tr_{opt}} \cdot \mathbf{tr_{tol}}$ **then**
13: **if** $\mathbf{tr_{opt}} - closest_{tr} < 0$ **then**
14: $closest_{lvl} \leftarrow$ decrease $closest_{lvl}$ to the closest lower level in **TVL**
15: **else**
16: $closest_{lvl} \leftarrow$ increase $closest_{lvl}$ to the closest higher level in **TVL**
17: **end if**
18: **end if**
19: **end for**

It would be ideal if the sum of intensities at the detectors were equal for all individual projections. However, since we are using different energy levels for different projections, this is not always the case. This can be an issue, during the reconstruction, since reconstruction algorithms typically assume a constant energy spectrum for acquiring the projections. To resolve this issue, we designed a sinogram equalization method. This algorithm uses the previously created optimized sinogram's intensities to create a scaling vector that can be used to equalize

the intensities for a proper reconstruction. We will refer to the sinogram created by the consecutive application of Alg. 2 and the sinogram equalization method as the *corrected-adaptive sinogram*.

### 5.2 Test environment

To conduct experiments, we used the GATE simulation software, an advanced open-source software developed by the international OpenGATE collaboration and dedicated to numerical simulations in medical imaging and radiotherapy. During the simulations, we used a polychromatic source, which can keep us closer to real applications. To simulate a perfect energy spectrum, we used Spekcalc, which is an executable for calculating the X-ray emission spectra from tungsten anodes such as those used in diagnostic radiology and kV radiotherapy X-ray tubes.

We used the following software phantoms. P1 was a perfect sphere on which we have shown how the transmission behaves if an object is not elongated, P2-P5 were elongated binary objects (with different length-width ratio and/or inner structure), and P6 was a self-made approximation of the well-known Forbild hip phantom[1]. For the reconstructions, we took the middle slices of these objects. In the GATE software, Phantoms P1-P5 were virtually made of PVC (Polyvinyl chloride). P6 consisted of the materials detailed in the description of the Forbild hip phantom.

After acquiring the projections, the reconstructions were performed using the Filtered Backprojection (FBP) technique. The quality of the reconstructions was evaluated by the Signal-to-noise ratio (SNR).

### 5.3 Results

We predefined 15 different energy levels. After generating the sinograms of all the phantoms on all the different energy levels, we calculated the SNR values belonging to the reconstructed slices. We refer to the sinograms of the reconstructions with the highest SNR values as the *original best sinograms*. The SNR values were also calculated for the reconstructed slices created using our *corrected-adaptive sinograms*, and we observed a slight increase in the SNR values in the case of almost every phantom.

Besides the slightly improved SNR values, another advantage of the adaptive voltage selection strategy is lower energy consumption, based on the fact that from certain angles, even a lower energy level could ensure optimal transmission. In the first and second row of Table 1, one can see the cumulated energies for creating the *original best* and the *corrected-adaptive sinogram*, respectively (using the mean energies of the different energy levels). Note that sinogram correction is simply achieved by executing the intensity equalization method, i.e., it does not affect cumulated energy. As we mentioned before, P1 is the perfect opposite of an elongated object. Therefore, the cumulated energy is the same in both cases. In all the other cases, the required energy for acquiring the *corrected-adaptive sinograms* is lower than it is needed for the *original best sinograms*. The percentages of the energy savings are shown in the third row. A significant energy reduction can be observed.

The findings of this thesis point have been published in a conference proceedings [11].

## 6 Convolutional Neural Networks in BT

The Artificial Neural Networks (ANNs) are based on the biological structure and behavior of the human brain, and the main application field for them is in Machine Learning. Convolutional Neural Networks (CNNs) are different from the structure of other neural networks since

[1] `http://www.imp.uni-erlangen.de/phantoms/index.htm`

Table 1: The cumulated energies needed for the *original best* and the *corrected-adaptive sinograms*, and the percentage of the saved energies, respectively.

| | **P1** | **P2** | **P3** | **P4** | **P5** | **P6** |
|---|---|---|---|---|---|---|
| *orig. best* [keV] | 11428.5 | 11428.5 | 11428.5 | 11428.5 | 10146 | 7638 |
| *corr. adapt.* [keV] | 11428.5 | 8930.4 | 10395 | 8930.4 | 8776.7 | 6906.1 |
| Saved energy [%] | 0 | 21.86 | 9.04 | 21.86 | 13.5 | 9.58 |

CNNs are mainly applied in the field of image processing and can also handle different types of input (e.g., image, video, voice).

In this thesis point, first, we show that neural networks are capable of solving a complex task like projection selection without any reconstruction step. Then, we provide a U-Net based segmentation algorithm for binarizing CT slices of different 3D printed specimens as part of an industrial project.

## 6.1 Proposed projection selection algorithm using CNNs

### 6.1.1 The workflow of the method

First, the CNN takes a sinogram ($180 \times 91$) as input (from the training database). After the 3 convolutional layers, a dense classifier connected to it outputs 180 activation values optimizing the MSE (Mean Squared Error) as the loss-function. These output values are thresholded to get the minimum number of projections required for each entity. Since we might end up with more than the required number of projections, a K-means clustering is applied to determine the exact angles to be used in the reconstruction process. Lastly, calculating the RME between the original image and the images reconstructed using the 3 methods explored here (labels, predictions, and equiangular projections) gives an estimate of the effectiveness of the selection procedure.

### 6.1.2 Evaluation and Results

Our image database consisted of 8983 phantoms (icons) of varying structural complexity, each with size $64 \times 64$ pixels. To create the training dataset, we performed a modified version of the *SFS* (Sequential Forward Selection) method (*Section 3.2*). This algorithm is referred to as *Label*. The main purpose of the projection selection procedures is to outperform the equiangular approaches by choosing the required angles in order to achieve a lower reconstruction error. Therefore, the results of the CNN based projection selection are compared to the results of the *Naive* method (*Section* 3.1) too. The proposed method will be denoted as *CNN*.

In Table 2, we present the RME and Standard Deviation (STD) values of the different methods with 4-6-8 angles, respectively. The •/◦ symbols highlight whether the differences are statistically significant (•) or not (◦), using a t-test with a significance level of 0.05. The results are statistically significant only with 8 projections. The RME values computed from the *Label* projection angles are naturally the smallest of the three, followed by our *CNN* approach. The equiangular approach produces the highest RMEs, meaning that the reconstructed images differed from the original ones the most using the *Naive* angle set. Using our 10-fold cross-validation test evaluations, we analyzed the RME values obtained using the 3 methods with 4 projections. We also present our findings in Table 3. We note here that these values are from the test set containing examples never encountered during the training of the model.

Table 2: Average of RME and Standard Deviation values calculated from 10 runs for the three different approaches. The significance values were computed pairwise for *Naive-Label*, *Label-CNN* and *Naive-CNN* and the significant statistical differences are presented column-wise with the symbols of •/◦.

| **4 projections** | *Label* | *CNN* | *Naive* |
|---|---|---|---|
| RME | 0.3817 ◦ | 0.4015 ◦ | 0.4912 ◦ |
| STD | 0.2078 | 0.2189 | 0.2903 |
| **6 projections** | *Label* | *CNN* | *Naive* |
| RME | 0.3196 ◦ | 0.3430 ◦ | 0.3866 ◦ |
| STD | 0.1723 | 0.1723 | 0.2341 |
| **8 projections** | *Label* | *CNN* | *Naive* |
| RME | 0.2746 • | 0.2940 • | 0.3128 • |
| STD | 0.1842 | 0.2174 | 0.2312 |

Table 3: The numbers of images on which the 3 distinct methods gave the smallest RME values are shown along the diagonal. The other cells show where two approaches gave the same RME value.

| **4 projections** | *Label* | *CNN* | *Naive* |
|---|---|---|---|
| *Label* | 4676 | 37 | 19 |
| *CNN* | 37 | 3096 | 14 |
| *Naive* | 19 | 14 | 1141 |

## 6.2 Segmentation of CT slices using CNNs

### 6.2.1 The workflow of the segmentation

For the segmentation of the CT-image slices, first, we trained a U-Net [21], using the original source code[2] (implemented in Tensorflow), provided by the authors. Depending on the task, 3-4 original slices (meaning less than 1 percent of the whole database) have been manually segmented to get golden standards (labels). The training data was formed by these few original CT-slices together with their corresponding golden standard binary masks. The test dataset consisted of the non-segmented slices. To increase the number of training images, the input data was cut into pixel patches of size $n \times n$, where $n$ is chosen from the interval $[50, 100]$ such that the remainder of the integer division $image\_width/n$ is the minimal possible. After the classification, the CT slices were reassembled from the patches.

The output of the network is a probability distribution, where the outputted values are expected to be very close to 0 or 1, so they can be interpreted as binary pixel values. As a post-processing step, a global thresholding was applied with different threshold values, and the qualitatively best has been chosen as the final binarized result.

After the examination of the results, given by the U-Net, we wanted to improve its performance. Therefore, we started to change the number of layers and the size of kernels in the U-Net architecture. All the different modifications we did were based on empirical tests. We modified some parts of the architecture, re-trained the model, generated the predictions and analyzed the resulted binary images. Then kept changing various parts based on the outcome. At the end of this process, the original architecture got modified quite significantly.

[2] `https://lmb.informatik.uni-freiburg.de/people/ronneber/u-net/`

Table 4: Comparison of different thresholding approaches using different quality measures

| | **PFOM** | **RAE** | **ME** | **HD** | **Average** |
|---|---|---|---|---|---|
| Otsu | 0.225 | 0.205 | 0.133 | 0.591 | 0.289 |
| Adaptive | 0.334 | 0.327 | 0.162 | 0.597 | 0.355 |
| Fuzzy C-means | 0.212 | 0.188 | 0.132 | 0.592 | 0.281 |
| Variational | 0.134 | 0.117 | 0.134 | 0.600 | 0.246 |
| U-Net | 0.105 | 0.093 | **0.084** | **0.559** | 0.210 |
| Proposed | **0.059** | **0.032** | 0.093 | 0.579 | **0.191** |

### 6.2.2 Evaluation and Results

Our segmentation approach was validated on two additively manufactured metal components, provided by Siemens AG. The full golden standard image set was given only for the second specimen. Therefore, this specimen was analyzed in detail from the image processing point of view and was compared to the results of other thresholding approaches.

We based our quantitative performance evaluation on a related research. In [23], the authors presented 40 segmentation techniques, and then ranked them based on 5 different criteria: misclassification error, edge mismatch, region nonuniformity, relative foreground area error, and shape distortion penalty via Hausdorff distance. We decided to use 4 measurements for this task. We used three propositions of [23]: misclassification error (**ME**), relative foreground area error (**RAE**), and shape distortion penalty via Hausdorff distance (**HD**). Instead of the edge mismatch, we used the mean-square distance figure of merit (**PFOM**) introduced by Pratt [19] because we found it a better measure for analyzing edges. We did not use region nonuniformity because it does not require ground-truth information, which could be misleading in this case.

Table 4 shows how the different thresholding methods performed based on the four different criteria. In the first column, one can see the thresholding approaches we used for the comparison. These methods are: Otsu method [17], local adaptive thresholding [2], variational minimax optimization based thresholding [22], fuzzy C-means [1], and the original U-Net. All the performance measures are adjusted so that their scores vary from 0 (for an entirely correct segmentation) to 1 (for an entirely erroneous case). Columns 2-5 contain the average scores over all the slices belonging to different quality measures in case of different segmentation techniques. To obtain an average performance, the authors of [23] suggested using the arithmetic average of the normalized scores defined above. The sixth column of Table 4 shows this average value. In every column, the smallest value is indicated with bold characters. One can see that U-Net and the proposed architecture can significantly outperform all the other techniques. In two of four measures, the U-Net performed better, while in the other two cases, the proposed architecture did. Taking the last (average) column into account, overall, the proposed approach seems to be the best one.

To compare the U-Net and the proposed architecture from another perspective, U-Net's total number of parameters is 1 940 817, while in the case of the proposed architecture, this number is only 566 657. This means that the proposed one consists of almost four times fewer parameters and can still provide at least as good results as the U-Net can, moreover, in most of the cases it can outperform U-Net.

The findings of this thesis point were in part published in a conference proceedings [18] and in a journal paper [8].

# 7 Summary of the author's contributions

The findings of the research can be divided into four thesis groups. Table 5 gives the connection between the results and the publications of the Author.

In the first thesis group, I proposed different sequential projection selection algorithms and analyzed their behavior under serious resolution down-scaling. These results were published in a conference proceedings [10], and in a journal paper [9].

I/1. I adapted and implemented sequential selection and search approaches to projection selection methods with almost fully deterministic behavior. I compared these methods to already published algorithms and showed with experimental tests that my algorithms could outperform the already existing approaches in this field.

I/2. I suggested two approaches to reduce the amount of data needed to select the most informative projection angles, and also examined how changing the scale of blueprint images and number of detectors affect the performance of projection selection algorithms. I developed and tested these approaches with the previously proposed projection selection methods. After the evaluation of the results, I proposed three different application fields where the scale invariance of projection selection could be used.

In the second thesis group, I embedded reconstruction uncertainty into projection selection algorithms and showed how grayscale uncertainty could be used in CT. These results were published in three conference proceedings [12, 13, 27], and are submitted as a journal paper [26].

II/1. I modified already implemented offline and online projection selection algorithms to embed the uncertainty as the optimization measure. I tested and compared them to already published algorithms. I showed that these algorithms can select the most informative projection angles by relying only on the reconstruction uncertainty, and even in the offline case, they do not require any blueprint data during the selection process.

II/2. I gave experimental validation to our results in the field of defining the grayscale uncertainty. I showed how the grayscale uncertainty could be used in the reconstruction of phantom images with continuous intensity interval and its correlation with the standard deviation of reconstructed pixel intensities, and how one can predict the upper and lower boundaries of the intensity values in practice. I also showed how the perturbed reconstructions could be used in practice to predict the reconstruction error that may arise during the reconstruction, which was followed by the evaluation of the results.

In the third thesis, group I proposed a transmission-based adaptive Automatic Tube Voltage Selection method for CT. The results of this thesis group were published in a conference proceedings [11].

III/1. I proposed an adaptive Automatic Tube Voltage Selection method complemented with a sinogram equalization algorithm for CT. I proposed to use only the transmission value of the sinogram to adjust the tube voltage on-the-fly during the acquisition and thus, to rely only on the projection data. By experimental tests on software simulated phantoms using the GATE toolbox, I found that this method is able to produce optimized sinograms and by that ensuring lower energy consumption and slightly better reconstruction quality. I pointed out that the presented method could be utilized in industrial non-destructive testing, and it has potential even in medical cases.

In the fourth thesis group, I proposed a CNN based offline projection selection algorithm and modified the well known U-Net architecture for the segmentation of CT images. The results of this thesis group were published in a conference proceedings [18], and in a journal paper [8].

IV/1. I proposed CNNs for projection selection to show that the most informative angles could be chosen without performing any reconstruction. I provided the theoretical background during this research from the tomographic point of view and the basis for the final angle selection algorithm. I modified the already existing projection selection algorithms to generate the training and test datasets. I compared the proposed method to state-of-the-art approaches and evaluated the results.

IV/2. I proposed CNNs for solving a particular segmentation problem as part of a bigger project. First, I used U-Net for the segmentations, then, modified its architecture to improve its performance. I generated the training and test datasets for this task. I compared my results to state-of-the-art segmentation techniques. Using different segmentation quality measures, I showed that my proposed model consists of almost four times fewer parameters and still provides at least as good results as the U-Net can. Still, in most of the cases, it can outperform U-Net.

Table 5: The connection between the thesis points and the Author's publications.

| | [10] | [9] | [12] | [13] | [27] | [26] | [11] | [18] | [8] |
|---|---|---|---|---|---|---|---|---|---|
| I/1. | • | | | | | | | | |
| I/2. | | • | | | | | | | |
| II/1. | | | • | • | | | | | |
| II/2. | | | | | • | • | | | |
| III/1. | | | | | | | • | | |
| IV/1. | | | | | | | | • | |
| IV/2. | | | | | | | | | • |

## References


[1] J. C. Bezdek, M. R. Pal, J. Keller, and R. Krisnapuram. *Fuzzy Models and Algorithms for Pattern Recognition and Image Processing*. Springer US, 1999. ISBN: 978-0-387-24579-9. DOI: 10.1007/b106267.

[2] R. C. Gonzalez and R. E. Woods. *Digital image processing*. Upper Saddle River, N.J.: Prentice Hall, 2008. ISBN: 9780131687288.

[3] M. A. Haque, M. O. Ahmad, M. N. S. Swamy, M. K. Hasan, and S. Y. Lee. "Adaptive Projection Selection for Computed Tomography". In: *IEEE Transactions on Image Processing* 22.12 (Dec. 2013), pp. 5085–5095. ISSN: 1057-7149. DOI: 10.1109/TIP.2013.2280185.

[4] G. T. Herman. *Fundamentals of Computerized Tomography: Image Reconstruction from Projections*. 2nd. Springer Publishing Company, Incorporated, 2009. ISBN: 9781852336172. DOI: 10.1007/978-1-84628-723-7.

[5] G. T. Herman and A. Kuba. *Advances in Discrete Tomography and Its Applications*. Birkhäuser Basel, 2007. DOI: 10.1007/978-0-8176-4543-4.

[6] G. T. Herman and A. Kuba. *Discrete Tomography: Foundations, Algorithms, and Applications*. Birkhäuser Basel, 1999. DOI: 10.1007/978-1-4612-1568-4.

[7] A. C. Kak and M. Slaney. *Principles of Computerized Tomographic Imaging*. IEEE Press, New York, 1988.

[8] N. Korshunova, J. Jomo, G. Lékó, D. Reznik, P. Balázs, and S. Kollmannsberger. "Image-based material characterization of complex microarchitectured additively manufactured structures". In: *Computers & Mathematics with Applications* 80 (11 2020), pp. 2462–2480. DOI: 10.1016/j.camwa.2020.07.018.

[9] G. Lékó and P. Balázs. "Scale Invariance in Projection Selection Using Binary Tomography". In: *Fundamenta Informaticae* 172.2 (2020), pp. 129–142. DOI: 10.3233/FI-2020-1897.

[10] G. Lékó and P. Balázs. "Sequential Projection Selection Methods for Binary Tomography". In: *Computational Modeling of Objects Presented in Images. Fundamentals, Methods, and Applications*. Ed. by R. P. Barneva, V. E. Brimkov, P. Kulczycki, and J. M. R. S. Tavares. Vol. 10986. Cham: Springer International Publishing, 2019, pp. 70–81. ISBN: 978-3-030-20805-9. DOI: 10.1007/978-3-030-20805-9_7.

[11] G. Lékó and P. Balázs. "Transmission Based Adaptive Automatic Tube Voltage Selection for Computed Tomography". In: *Combinatorial Image Analysis*. Ed. by T. Lukić, R. P. Barneva, V. E. Brimkov, L. Čomić, and N. Sladoje. Vol. 12148. Cham: Springer International Publishing, 2020, pp. 199–208. ISBN: 978-3-030-51002-2. DOI: 10.1007/978-3-030-51002-2_14.

[12] G. Lékó, P. Balázs, and L. G. Varga. "Projection Selection for Binary Tomographic Reconstruction Using Global Uncertainty". In: *Image Analysis and Recognition*. Ed. by A. Campilho, F. Karray, and B. ter Haar Romeny. Vol. 10882. Cham: Springer International Publishing, 2018, pp. 3–10. ISBN: 978-3-319-93000-8. DOI: 10.1007/978-3-319-93000-8_1.

[13] G. Lékó, S. Domány, and P. Balázs. "Uncertainty Based Adaptive Projection Selection Strategy for Binary Tomographic Reconstruction". In: *Computer Analysis of Images and Patterns*. Ed. by M. Vento and G. Percannella. Vol. 11679. Cham: Springer International Publishing, 2019, pp. 74–84. ISBN: 978-3-030-29891-3. DOI: 10.1007/978-3-030-29891-3_7.

[14] N. Metropolis, A. W. Rosenbluth, M. N. Rosenbluth, A. H. Teller, and E. Teller. "Equation of State Calculations by Fast Computing Machines". In: *The Journal of Chemical Physics* 21.6 (1953), pp. 1087–1092. DOI: 10.1063/1.1699114.

[15] L. C. Molina, L. Belanche, and A. Nebot. "Feature selection algorithms: a survey and experimental evaluation". In: *2002 IEEE International Conference on Data Mining, 2002. Proceedings*. 2002, pp. 306–313. DOI: 10.1109/ICDM.2002.1183917.

[16] A. Nagy and A. Kuba. "Reconstruction of binary matrices from fan-beam projections". In: *Acta Cybernetica* 17.2 (2005), pp. 359–385.

[17] N. Otsu. "A Threshold Selection Method from Gray-Level Histograms". In: *IEEE Transactions on Systems, Man, and Cybernetics* 9.1 (1979), pp. 62–66. DOI: 10.1109/TSMC.1979.4310076.

[18] G. Pap, G. Lékó, and T. Grósz. "A Reconstruction-Free Projection Selection Procedure for Binary Tomography Using Convolutional Neural Networks". In: *Image Analysis and Recognition*. Ed. by F. Karray, A. Campilho, and A. Yu. Vol. 11662. Cham: Springer International Publishing, 2019, pp. 228–236. ISBN: 978-3-030-27202-9. DOI: 10.1007/978-3-030-27202-9_20.

[19] W. K. Pratt. *Digital Image Processing*. New York, Wiley-Interscience, 1978.

[20] P. Pudil, J. Novovičová, and J. Kittler. "Floating search methods in feature selection". In: *Pattern Recognition Letters* 15.11 (1994), pp. 1119–1125. DOI: 10.1016/0167-8655(94)90127-9.

[21] O. Ronneberger, P. Fischer, and T. Brox. "U-Net: Convolutional Networks for Biomedical Image Segmentation". In: *Medical Image Computing and Computer-Assisted Intervention*. Ed. by N. Navab, J. Hornegger, W. M. Wells, and A. F. Frangi. Cham: Springer International Publishing, 2015, pp. 234–241. DOI: 10.1007/978-3-319-24574-4_28.

[22] B. N. Saha and N. Ray. "Image Thresholding by Variational Minimax Optimization". In: *Pattern Recogn.* 42.5 (May 2009), 843—856. ISSN: 0031-3203. DOI: 10.1016/j.patcog.2008.09.033.

[23] M. Sezgin and B. Sankur. "Survey over image thresholding techniques and quantitative performance evaluation". In: *Journal of Electronic Imaging* 13 (Jan. 2004), pp. 146–168. DOI: 10.1117/1.1631315.

[24] L. Varga, P. Balázs, and A. Nagy. "Direction-dependency of binary tomographic reconstruction algorithms". In: *Graphical Models* 73.6 (2011). Computational Modeling in Imaging Sciences, pp. 365–375. ISSN: 1524-0703. DOI: 10.1016/j.gmod.2011.06.006.

[25] L. Varga, P. Balázs, and A. Nagy. "Projection Selection Algorithms for Discrete Tomography". In: *Advanced Concepts for Intelligent Vision Systems*. Ed. by J. Blanc-Talon, D. Bone, W. Philips, D. Popescu, and P. Scheunders. Berlin, Heidelberg: Springer Berlin Heidelberg, 2010, pp. 390–401. ISBN: 978-3-642-17688-3. DOI: 10.1007/978-3-642-17688-3_37.

[26] L. G. Varga, G. Lékó, and P. Balázs. "Grayscale Uncertainty and Errors of Tomographic Reconstructions Based on Projection Geometries and Projection Sets". In: ***Submitted*** *to Journal of Combinatorial Optimization - SI: Combinatorial Optimization in Imaging Sciences* (2020).

[27] L. G. Varga, G. Lékó, and P. Balázs. "Grayscale Uncertainty of Projection Geometries and Projections Sets". In: *Combinatorial Image Analysis*. Ed. by T. Lukić, R. P. Barneva, V. E. Brimkov, L. Čomić, and N. Sladoje. Vol. 12148. Cham: Springer International Publishing, 2020, pp. 123–138. ISBN: 978-3-030-51002-2. DOI: 10.1007/978-3-030-51002-2_9.

[28] L. G. Varga, L. G. Nyúl, A. Nagy, and P. Balázs. "Local and global uncertainty in binary tomographic reconstruction". In: *Computer Vision and Image Understanding* 129 (2014). Special section: Advances in Discrete Geometry for Computer Imagery, pp. 52–62. ISSN: 1077-3142. DOI: 10.1016/j.cviu.2014.05.006.

[29] A. Watson. "Perimetric Complexity of Binary Digital Images". In: *The Mathematica Journal* 14 (Mar. 2012).

# Publications of the Author

## Journal publications

- Gábor Lékó and Péter Balázs. "Detecting Steel Cord Discontinuities in Tire Tread X-Ray Images: A Preliminary Study". International Journal of Circuits, Systems and Signal Processing (NAUN) 11 314-318 (2017), ISSN: 1998-4464. SJR: Q4
- Gábor Lékó and Péter Balázs. "Scale Invariance in Projection Selection Using Binary Tomography". In: Fundamenta Informaticae 172.2 (2020), pp. 129–142. DOI: 10.3233/FI-2020-1897. IF: 1.204. SJR: Q3
- Nina Korshunova, John Jomo, Gábor Lékó, Daniel Reznik, Péter Balázs and Stefan Kollmannsberger. "Image-based material characterization of complex microarchitectured additively manufactured structures". In: Computers & Mathematics with Applications 80 (11 2020), pp. 2462–2480. ISSN: 0898-1221. DOI: 10.1016/j.camwa.2020.07.018. IF: 3.370. SJR: Q1
- László G. Varga, Gábor Lékó, and Péter Balázs. "Grayscale Uncertainty and Errors of Tomographic Reconstructions Based on Projection Geometries and Projection Sets". *In:* ***Submitted*** *to Journal of Combinatorial Optimization - SI: Combinatorial Optimization in Imaging Sciences* (2020). IF: 0.843. SJR: Q2

## Full papers in conference proceedings

- Gábor Lékó, Péter Balázs, and László G. Varga. "Projection Selection for Binary Tomographic Reconstruction Using Global Uncertainty". In: Image Analysis and Recognition. Ed. by Aurélio Campilho, Fakhri Karray, and Bart ter Haar Romeny. Vol. 10882. Cham: Springer International Publishing, 2018, pp. 3–10. ISBN: 978-3-319-93000-8. DOI: 10.1007/978-3-319-93000-8_1. CORE: C
- Gábor Lékó and Péter Balázs. "Sequential Projection Selection Methods for Binary Tomography". In: Computational Modeling of Objects Presented in Images. Fundamentals, Methods, and Applications. Ed. by Reneta P. Barneva et al. Vol. 10986. Cham: Springer International Publishing, 2019, pp. 70–81. ISBN: 978-3-030-20805-9. DOI: 10.1007/978-3-030-20805-9_7.
- Gábor Lékó, Szilveszter Domány, and Péter Balázs. "Uncertainty Based Adaptive Projection Selection Strategy for Binary Tomographic Reconstruction". In: Computer Analysis of Images and Patterns. Ed. by Mario Vento and Gennaro Percannella. Vol. 11679. Cham: Springer International Publishing, 2019, pp. 74–84. ISBN: 978-3-030-29891-3. DOI: 10.1007/978-3-030-29891-3_7. CORE: B
- Gergely Pap, Gábor Lékó, and Tamás Grósz. "A Reconstruction-Free Projection Selection Procedure for Binary Tomography Using Convolutional Neural Networks". In: Image Analysis and Recognition. Ed. by Fakhri Karray, Aurélio Campilho, and Alfred Yu. Vol. 11662. Cham: Springer International Publishing, 2019, pp. 228–236. ISBN: 978-3-030-27202-9. DOI: 10.1007/978-3-030-27202-9_20. CORE: C
- Gábor Lékó and Péter Balázs. "Transmission Based Adaptive Automatic TubeVoltage Selection for Computed Tomography". In: Combinatorial Image Analysis. Ed. by Tibor Lukić et al. Vol. 12148. Cham: Springer International Publishing, 2020, pp. 199–208. ISBN: 978-3-030-51002-2. DOI: 10.1007/978-3-030-51002-2_14. CORE: C
- László G. Varga, Gábor Lékó, and Péter Balázs. "Grayscale Uncertainty of Projection Geometries and Projections Sets". In: Combinatorial Image Analysis. Ed. by Tibor Lukić et al. Vol. 12148. Cham: Springer International Publishing, 2020, pp. 123–138. ISBN: 978-3-030-51002-2. DOI: 10.1007/978-3-030-51002-2_9. CORE: C

## Other publications

- Péter Balázs, Gábor Lékó, Zoltán Ozsvár, Gábor Petrovszki, Judit Szűcs, László Varga: Design and implementation of the informatical system of a 3D industrial CT scanner, Abstracts of the 11th Conference of the Hungarian Association of Image Processing and Pattern Recognition, Szováta, Romania, 24-27 January, 2017, 10 pages (in Hungarian).
- Gábor Lékó, Péter Balázs, László G. Varga: Projection selection using uncertainty in binary tomogrpahy, Abstracts of the 5th Winter School of PhD Students in Informatics and Mathematics, Debrecen, Hungary, 2-4 March, 2018, pp. 30.
- Gábor Lékó, Péter Balázs, László G. Varga: Projection selection with sequential selection methods using different evaluation measures, Volume of Short Papers of the 11th Conference of PhD Students in Computer Science, Szeged, Hungary, 25-27 June, 2018, pp. 79.
- Gábor Lékó, Péter Balázs, László G. Varga: Sequential projection selection methods and global uncertainty in projection selection, Abstracts of the 12th Conference of the Hungarian Association of Image Processing and Pattern Recognition, Debrecen, Hungary, 28-31 January, 2019, 15 pages (in Hungarian).